Narrowing the Mass Range of Fuzzy Dark Matter with Ultrafaint Dwarfs

Kohei Hayashi[1,2] , Elisa G. M. Ferreira[3,4] , and Hei Yin Jowett Chan[1]
[1] Astronomical Institute, Tohoku University, Sendai, Miyagi, 980-8578, Japan; k.hayasi@astr.tohoku.ac.jp, jchan@astr.tohoku.ac.jp
[2] National Institute of Technology, Ichinoseki College, Takanashi, Hagisho, Ichinoseki, Iwate, 021-8511, Japan
[3] Max Planck Institute for Astrophysics, Karl-Schwarzschild-Str. 1, D-85748 Garching, Germany
[4] Instituto de Física, Universidade de São Paulo, C.P. 66318, 05315-970, São Paulo, SP, Brazil; elisagmf@mpa-garching.mpg.de

Abstract

Fuzzy dark matter (FDM) is an attractive dark matter candidate motivated by small-scale problems in astrophysics and with a rich phenomenology on those scales. We scrutinize the FDM model, more specifically the mass of the FDM particle, through a dynamical analysis for the Galactic ultrafaint dwarf (UFD) galaxies. We use a sample of 18 UFDs to place the strongest constraints to date on the mass of the FDM particle, updating on previous bounds using a subset of the sample used here. We find that most of the sample UFDs prefer an FDM particle mass heavier than 10^{-21} eV. In particular, Segue 1 provides the strongest constraint, with $m_\psi = 1.1^{+8.3}_{-0.7} \times 10^{-19}$ eV. The constraints found here are the first that are compatible with various other independent cosmological and astrophysical bounds found in the literature, in particular with the latest bounds using the Lyα forest. We also find that the constraints obtained in this work are not compatible with the bounds from luminous dwarf galaxies, as already pointed out in the previous work using UFDs. This could indicate that although a viable dark matter model, it might be challenging for the FDM model to solve the small-scale problems.

Unified Astronomy Thesaurus concepts: Dark matter (353); Galaxy dynamics (591); Dwarf spheroidal galaxies (420)

1. Introduction

The fuzzy dark matter (FDM) model (e.g., Hu et al. 2000) recently emerged as an alternative that can solve the small-scale challenges to the cold dark matter (CDM) model, while preserving the behavior of CDM on large scales. Due to its ultralight mass and bosonic nature, FDM exhibits a wave-like behavior on Galactic scales that leads to cosmological and astrophysical consequences. The effects of these on different observables allows us to constrain the one and only parameter, the particle mass m_ψ of the FDM model (for reviews on these effects see Ferreira 2020; Hui 2021).

The proposed mass range for which the FDM produces a solitonic core in the interior of galaxies, thus addressing the "core–cusp" problem, is of the order of $m_\psi \sim 10^{-22}$ eV (Hui et al. 2017). However, the current observations are pushing the lower bound to heavier particle masses. The suppression in the matter power spectrum induced by FDM can be measured by the Lyα forest observations, and has put a lower bound of $m_\psi \gtrsim 10^{-20}$ eV (Rogers & Peiris 2021). These bounds are in tension with the previously expected canonical value of m_ψ required to solve the small-scale problem.

The dwarf spheroidal galaxies (dSphs), as a dark-matter-dominated system, are the promising astrophysical probes of the nature of dark matter. The stellar kinematic data of the dSphs therefore enable us to place constraints on the particle mass based on the dynamical analysis (Schive et al. 2014; Chen et al. 2017; González-Morales et al. 2017; Hayashi & Obata 2020). However, several groups have suggested that dark matter density profiles in the luminous dSphs could be affected by baryonic physics (e.g., Read et al. 2019; Hayashi et al. 2020). For the ultrafaint dwarf (UFD) galaxies, which host much smaller stellar masses than the luminous ones, the impact of baryonic feedback on their inner dark matter densities can be negligible (e.g., Lazar et al. 2020) and thus the UFDs are ideal targets to derive reliable constraints on the FDM model. Nevertheless, only a few have studied the FDM model by UFDs. Using

the measurement of half-light masses of two UFDs, Draco II and Triangulum II, a mass estimate of $m_\psi \sim 3.7$–5.6×10^{-22} eV was obtained by Calabrese & Spergel (2016). In Safarzadeh & Spergel (2020), using Milky Way UFDs, a bound on m_ψ was obtained, $m_\psi > 10^{-21}$ eV. This bound was compared with the bounds from the analysis of luminous dSphs, showing that they are in tension with each other. As more stellar kinematic data of UFDs become available, it is essential to perform a full Jeans analysis to update the constraint on m_ψ.

In this Letter, we perform the Jeans analysis of the stellar kinematic data of 18 UFDs to constrain m_ψ. We show that these systems prefer m_ψ that is higher than the canonical expectation of the FDM. We compare our mass constraints to the most relevant bounds that exist in the literature and found that they are compatible within uncertainties. Among the UFDs, Segue 1 provides the strongest constraint, which challenges the proposed canonical mass range of the FDM model with $m_\psi \sim 10^{-22}$–10^{-21} eV.

2. Models

To constrain m_ψ, we adopt here the spherical Jeans equation, which relates a stellar phase-space distribution to a dark matter halo mass distribution. For a spherically symmetric system in dynamical equilibrium, this is given by Binney & Tremaine (2008):

$$\frac{\partial[\nu(r)\sigma_r^2(r)]}{\partial r} + \frac{2\nu(r)\beta_{\mathrm{ani}}(r)\sigma_r^2(r)}{r} = -\nu(r)\frac{GM(r)}{r^2}, \quad (1)$$

where r denotes the radius from the center of a system, $\nu(r)$ is the three-dimensional stellar density distribution, G is the gravitational constant, and $M(r)$ is the dark matter mass distribution. The stellar velocity ellipsoid defined by (σ_r, σ_θ, σ_ϕ) is equated with spherical coordinates. Since $\sigma_\theta = \sigma_\phi$ for spherical symmetry, the stellar velocity anisotropy is written as $\beta_{\mathrm{ani}}(r) \equiv 1 - \sigma_\theta^2(r)/\sigma_r^2(r)$. Here, we adopt a general and

realistic stellar anisotropy model proposed by Baes & Van Hese (2007):

$$\beta_{\rm ani}(r) = \frac{\beta_0 + \beta_\infty (r/r_\beta)^\eta}{1 + (r/r_\beta)^\eta}, \qquad (2)$$

where β_0 and β_∞ are the inner and outer anisotropy parameters. The spatial dependence of $\beta_{\rm ani}$ is characterized by the transition sharpness η and radius r_β.

To compare observed line-of-sight velocity dispersion profiles with the model, we project the radial dispersion profile from Equation (1) into the line-of-sight direction:

$$\Sigma(R)\sigma_{\rm los}^2(R) = 2\int_R^\infty dr \left(1 - \beta_{\rm ani}(r)\frac{R^2}{r^2}\right) \frac{\nu(r)\sigma_r^2(r)}{\sqrt{1 - R^2/r^2}}, \quad (3)$$

where R is the projected radius, $\Sigma(R)$ is the projected stellar density profile derived from the intrinsic stellar density $\nu(r)$, and $\sigma_{\rm los}$ is the line-of-sight velocity dispersion. In this work, we assume the Plummer profile for the stellar density profile (Plummer 1911), $\Sigma(R) = (\pi r_{\rm half}^2)^{-1}[1 + R^2/r_{\rm half}^2]^{-2}$, where $r_{\rm half}$ is the projected half-light radius.

FDM can form a soliton core in the central parts of a galaxy, which corresponds to the ground state solution of the Schrödinger–Poisson equation. Owing to high-resolution FDM simulations (e.g., Schive et al. 2014), the radial profile of the soliton core can be written analytically:

$$\rho_{\rm soliton}(r) = \frac{\rho_c}{[1 + 0.091(r/r_c)^2]^8}, \qquad (4)$$

where r_c is the soliton core radius and ρ_c is the central density given by

$$\rho_c = 1.9 \times 10^{12}\left(\frac{m_\psi}{10^{-23}\,{\rm eV}}\right)^{-2}\left(\frac{r_c}{\rm pc}\right)^{-4}\,[M_\odot\,{\rm pc}^{-3}]. \quad (5)$$

The mass profile, $M_{\rm soliton}(r) = \int_0^r 4\pi\,s^2\rho(s)ds$, also can be calculated analytically (Chen et al. 2017). The simulations also predicted the scaling relation between a soliton core radius, particle mass, and dark halo mass,

$$r_c \simeq 1600\left(\frac{m_\psi}{10^{-23}{\rm eV}}\right)^{-1}\left(\frac{M_{200}}{10^{12}M_\odot}\right)^{-1/3}\,{\rm pc}, \qquad (6)$$

where M_{200} is the enclosed mass within r_{200} in which the spherical overdensity is 200 times the critical density of the universe. We thus determine the soliton core radius r_c, given m_ψ and M_{200} as free parameters.

Beyond the core radius, the halo profile is akin to a Navarro–Frenk–White (NFW) profile (Navarro et al. 1997),

$$\rho_{\rm NFW}(r) = \frac{\rho_s}{(r/r_s)(1 + r/r_s)^2}. \qquad (7)$$

To transition from the central soliton core to the outer NFW halo, we impose a density continuity condition at the radius r_ϵ,

$$\frac{\rho_s}{(r_\epsilon/r_s)(1 + r_\epsilon/r_s)^2} = \frac{\rho_c}{[1 + 0.091(r_\epsilon/r_c)^2]^8} = \epsilon\rho_c, \quad (8)$$

and r_ϵ can be derived as $r_\epsilon = (0.091)^{-1/2}r_c(\epsilon^{-1/8} - 1)^{1/2}$. Thus, when ϵ and r_s are given, ρ_s can be determined. According to the numerical simulations (Schive et al. 2014; Mocz et al. 2018), r_ϵ should be larger than $3r_c$.

The halo with a heavier m_ψ has a very small core and most of the halo is described by an NFW profile. Since a large part of the halo has a similar behavior to a CDM halo, we impose the concentration–mass relation of the NFW halos predicted by CDM simulations:

$$C_{200}(M_{200}, x_{\rm sub}) = c_0\left[1 + \sum_{i=1}^3\left[a_i\log_{10}\left(\frac{M_{200}}{10^8 h^{-1}M_\odot}\right)\right]^i\right] \\ \times [1 + b\log_{10}(x_{\rm sub})]. \quad (9)$$

Here, we utilize $c_0 = 19.9$, $a_i = \{-0.195, 0.089, 0.089\}$, and $b = -0.54$, which are the best-fit parameters for the concentration–mass relation (Moliné et al. 2017). The subhalo distance from the center of a host halo divided by r_{200} of the host halo is given by $x_{\rm sub} \equiv r_{\rm sub}/r_{200,\rm host}$. The r_{200} of the Milky Way halo, $r_{200,\rm MW}$, has a large uncertainty $r_{200} \simeq 210 \pm 50$ kpc. However, the error of $r_{200,\rm MW}$ may not have impact on the concentration parameter. Therefore, we adopt $r_{200,\rm MW} = 210$ kpc in this work. [5]

3. Data and Analysis

To scrutinize FDM halos of the Milky Way UFDs, we select 18 galaxies (Boötes I, Coma Bernices, Canes Venatici I, Canes Venatici II, Eridanus II, Grus 2, Hercules, Hydra II, Leo IV, Reticulum II, Segue 1, Segue 2, Triangulum II, Tucana 3, Tucana 4, Ursa Major I, Ursa Major II, and Willman 1). They have more than 10 stellar kinematic data of their member stars.

The stellar structural parameters of these galaxies are taken from Drlica-Wagner et al. (2015) and Muñoz et al. (2018). For the stellar kinematic sample analyzed in the present study, we use the published data from the original spectroscopic observation papers (Simon & Geha 2007; Simon et al. 2011; Willman et al. 2011; Kirby et al. 2013, 2015; Simon et al. 2015; Kirby et al. 2017; Simon et al. 2017, 2020; Jenkins et al. 2020; Zoutendijk et al. 2021). To identify the member stars, we adopt the methods in the above literature. For the influence of unresolved binary stars on a stellar kinematics, several papers indicated that multiepoch observations can exclude binary candidates from stellar spectroscopic data and concluded that the presence of binaries is likely to have only mild influence on estimates of the velocity dispersion of UFDs. Thus, we ignore this effect.

Given the available observational data, we fit models for $\rho_{\rm soliton}(r) + \rho_{\rm NFW}(r)$ and $\beta_{\rm ani}(r)$ with the likelihood function $\log(\mathcal{L}_{\rm tot}) = \log(\mathcal{L}_{\rm vel}) + \log(\mathcal{L}_{\rm NFW}) + \log(\mathcal{L}_{r_{\rm half}})$. We assume that the line-of-sight velocity distribution is a Gaussian; thus, the likelihood function coming from the stellar kinematics is written by

$$-2\log(\mathcal{L}_{\rm vel}) = \sum_i\left[\frac{(v_i - \langle v \rangle)^2}{\sigma_i^2} + \log(2\pi\sigma_i^2)\right], \quad (10)$$

where v_i and R_i are the line-of-sight velocity and the projected radius from the center of the galaxy of the ith star in the kinematic sample. The averaged line-of-sight velocity of the member stars $\langle v \rangle$ is a nuisance parameter. The dispersion σ_i^2 can be written by the measurement error $\delta_{v,i}$ and the intrinsic dispersion: $\sigma_i^2 = \delta_{v,i}^2 + \sigma_{\rm los}^2(R_i)$.

---

[5] We performed the same MCMC analyses for the case of $r_{200,\rm MW} = 160$ and 260 kpc and obtained $m_\psi = 1.0^{+8.6}_{-0.6} \times 10^{-19}$ eV and $1.1^{+8.8}_{-0.7} \times 10^{-19}$ eV, respectively. Thus, we confirmed the uncertainty on $r_{200,\rm MW}$ can be negligible.
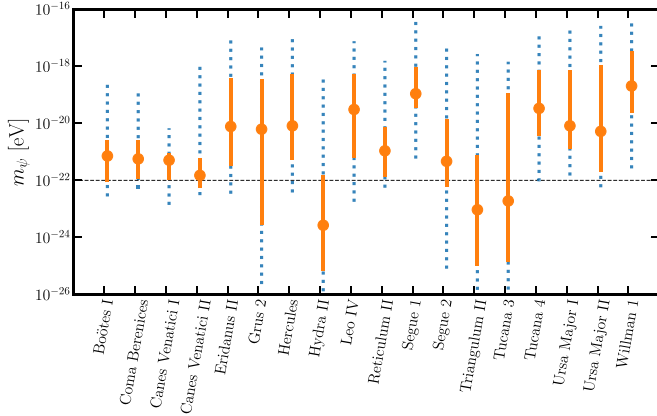
Figure 1. Estimated FDM mass, m_ψ, for 17 UFDs. The points show the median values of m_ψ, and orange solid and blue dotted errors are 1σ and 2σ credible intervals. The horizontal dashed line corresponds to $m_\psi = 10^{-22}$ eV.

Meanwhile, we require the outer NFW halo to satisfy the concentration–mass relation; thus, the likelihood is given by

$$-2\log(\mathcal{L}_{\text{NFW}}) = \frac{[\log_{10}(c_{200}) - \log_{10}(C_{200})]^2}{\sigma_{\text{CDM}}^2}. \qquad (11)$$

We estimate c_{200} from the parameters (r_s, ρ_s, M_{200}), and C_{200} is the median subhalo concentration–mass relation in Equation (9) with $\sigma_{\text{CDM}} = 0.13$ (Moliné et al. 2017).

We also consider the uncertainties of the half-light radius (r_{half}) of the Plummer profile as the following form: $-2\log(\mathcal{L}_{r_{\text{half}}}) = (r_{\text{half}} - r_{\text{half,obs}})^2 / \delta r_{\text{half,obs}}^2$, where $r_{\text{half,obs}}$ and $\delta r_{\text{half,obs}}$ are the measured half-light radius and its error based on the photometric data.

Our model has 10 free parameters (m_ψ, M_{200}, ϵ, r_s, β_0, β_∞, r_β, η, r_{half}, and $\langle v \rangle$). We adopt flat priors over the following ranges: $-3 \leqslant \log_{10}(m_\psi/10^{-23}\text{eV}) \leqslant 8$, $8 \leqslant \log_{10}(M_{200}/M_\odot) \leqslant 11$, $-5 \leqslant \log_{10}(\epsilon) \leqslant \log_{10}(0.5)$, $0 \leqslant \log_{10}(r_{s,\beta}/[\text{pc}]) \leqslant 4$, $1 \leqslant \eta \leqslant 10$, $0 \leqslant 2^{\beta_{0(\infty)}} \leqslant 1(2)$, $0 \leqslant r_{\text{half}}/\text{pc} \leqslant 1000$, and $-1000 \leqslant \langle v \rangle/(\text{km s}^{-1}) \leqslant +1000$. For the range of M_{200}, several numerical studies implied that UFD-sized galaxies ($L_* \sim 10^{2.5-5.0}L_\odot$) reside in dark matter halos of mass $M_{200} \sim 10^8 - 10^9 M_\odot$ (e.g., Wheeler et al. 2015). To obtain conservative limits on m_ψ, we however adopt the heavier upper limit of this prior range. We map the posterior distributions of these parameters using the public python package emcee (Foreman-Mackey et al. 2013). For each galaxy, we set the sampler to 280 walkers and 6000 steps and removed 1000 steps as burn-in.

4. Results and Discussion

In Figure 1, we show the estimated m_ψ, from all galaxies. The median, 1σ and 2σ credible intervals are computed from the posterior probability distribution functions (PDFs). We find that even though there surely exist large uncertainties on m_ψ, caused by a small sample size, the majority of the UFDs favor $m_\psi \gtrsim 10^{-22}$ eV (the horizontal dashed line in this figure), which was considered the key particle mass to resolve the core–cusp problem (e.g., Marsh & Pop 2015). In particular, the fitting result for Segue 1 shows the significantly large FDM mass, $m_\psi = 1.1^{+8.3(+403)}_{-0.7(-1.1)} \times 10^{-19}$ eV, at 1σ and 2σ credible intervals. [6] These results show that the soliton core in UFDs is
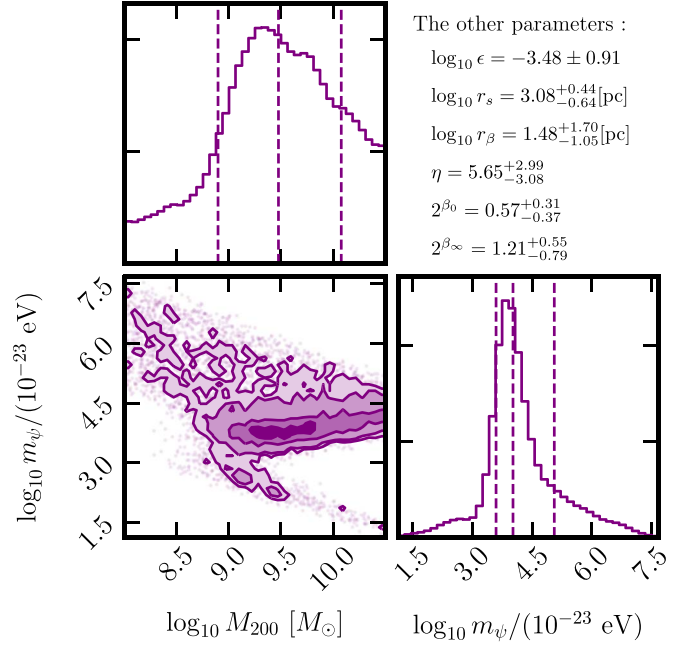

Figure 2. Posterior distributions of M_{200} and m_ψ for Segue 1. The dashed vertical lines in the 1D histograms are the median and 1σ credible intervals. At the upper right corner, the other parameters (the median and 1σ credible intervals) are indicated.

very small, which confirms the existence of a large NFW outer halo around the solitonic core, supporting the profile used in the fit of this work.

Figure 2 shows the posterior PDFs of Segue 1. To focus on m_ψ, we show the posteriors of M_{200} and m_ψ only, while the other parameters are indicated at the upper right corner. As shown in this figure, m_ψ can be constrained statistically by our analysis. Note that the constraint on m_ψ from Segue 1 comes mainly from the kinematic sample in the inner part (especially within 10 pc) in our unbinned analysis. The unbinned analysis can trace the inner kinematic structures in the UFDs, while the binned one might smear out such information, and thus may not provide such a strong constraint on m_ψ as the unbinned one.

It is important to understand how the constraints obtained here relate to the bounds obtained from the other independent work. This is shown in Figure 3, where we compare our constraint on m_ψ from Segue 1, the strongest constraint obtained from this work, shown in red, with a selection of the strongest ones compiled in the review paper (Ferreira 2020).[7]

The blue shaded regions represent the values of m_ψ that are currently excluded by analysis of the corresponding observations. In this figure we also show the previous bounds obtained using UFDs from Safarzadeh & Spergel (2020) and Marsh & Niemeyer (2019).

We find that the constraint on m_ψ for Segue 1 falls in the allowed region of the other observations like cosmic microwave background, large-scale structure, and black hole superradiance (BHSR) from M87 and supermassive BHs (SMBHs), even though there is a slight tension with the bound from BHSR from SMBHs. This result is also compatible with the previous bounds obtained using UFDs, updating on these bounds and obtaining stronger constraints in m_ψ. Our result from Segue 1 is allowed even considering the bounds from

---

[6] The estimated dark halo mass, M_{200}, for Segue 1 is $\log_{10}(M_{200}/M_\odot) = 9.6^{+0.74}_{-0.68}$ at 1σ credible intervals.

[7] There are also other strong constraints not shown here like Schutz (2020) and Nadler et al. (2021).
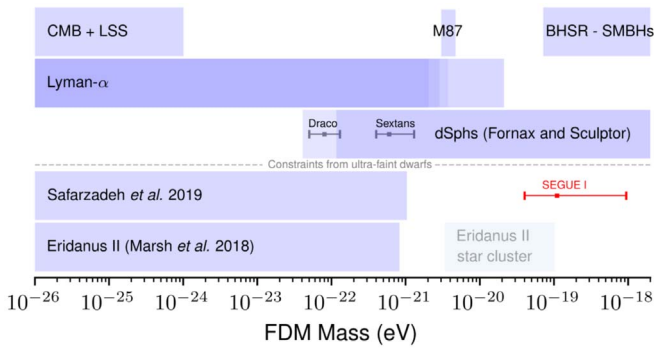
Figure 3. Summary of the most relevant constraints on the FDM mass to date. The blue shaded regions represent the excluded regions. We highlight in red the constraint for Segue 1 from this work. The first line presents the bounds from cosmic microwave background (CMB) and large-scale structure (LSS) from Hlozek et al. (2015, 2018), and those from black hole superradiance (BHSR) from supermassive BH (SMBH) in M87 (Davoudiasl & Denton 2019) and from SMBHs (Stott & Marsh 2018). The second line presents the bounds from Lyα observations (Armengaud et al. 2017; Iršič et al. 2017; Nori et al. 2019; Rogers & Peiris 2021), from darker to lighter. The bounds from dSphs come from Fornax and Sculptor given in González-Morales et al. (2017, darker) and Marsh & Pop (2015, lighter), and two constraints with error bars are from Draco and Sextans (Chen et al. 2017). Bellow the dashed line we present the previous and current constraints using UFDs from Safarzadeh & Spergel (2020), and from Eridanus II by Marsh & Niemeyer (2019).

Lyα measurements, which was to date the strongest bounds requiring $m_\psi > 2 \times 10^{-20}$ eV, and the first constraint compatible with this bound. Although not shown in the figure, this is also true for the constraints obtained from the other 17 UFDs, which are all compatible with these bounds within the uncertainty in their mass constraint.

The Segue 1 constraint seems to be in tension with the ones from the survival of the Eri II star cluster ("Eridanus II—star cluster" in Figure 3), although compatible with the condition for the existence of a subhalo to host Eri II, $m_\psi > 8 \times 10^{-22}$ eV (Marsh & Niemeyer 2019). The survival bound comes from gravitational heating due to the solitonic core. This has recently been challenged (Schive et al. 2020), where heating is reduced by tidal disruption of the halo, allowing for the survival of the star cluster for higher m_ψ like ours. Future simulations are necessary to verify this effect.

The constraint obtained from Segue 1, however, is in tension with the bounds coming from luminous dSphs, Fornax and Sculptor. These bounds require $m_\psi < 2.9$–4×10^{-21} eV (González-Morales et al. 2017; Marsh & Pop 2015). Our constraints fall in the excluded region of m_ψ from the luminous dSphs, which is also in tension with the bounds from other observations. The same conclusion was found in Safarzadeh & Spergel (2020) where a comparative analysis of the constraints on m_ψ using data of the half-light radius of dSphs and UFDs was made, using a subgroup of the UFDs using here. Therefore, m_ψ found from the analysis of UFDs cannot explain the density profile of Fornax and Sculptor. This might be indicative that it is challenging for the FDM to address the small-scale problems of the CDM model. This was also pointed out, in the context of the cusp–core problem, using a different argument in Burkert (2020).

However, we note that these luminous dSphs could have been affected by baryonic processes. This can change the density structure of their halo, meaning that we are not probing the intrinsic dark matter profile. This might challenge the bounds coming from

these systems. As discussed in Safarzadeh & Spergel (2020), the FDM soliton profile might be too simplistic, and if allowed to change for different systems, which might also depend on the baryonic effects, would allow a more realistic description of the core of different systems and lead to different bounds on m_ψ. In this sense, Milky Way UFDs are ideal objects to probe the nature of DM theory, making us believe that the results presented in this work are a robust measure of the properties of the FDM.

We should also emphasize that our work is based on a fit to a profile for the halo that consists of a soliton core surrounded by an NFW profile, with the relation between the core mass and the halo mass given in Schive et al. (2014). However, different simulations (Mocz et al. 2017; Mina et al. 2020) report a different relation (although the analysis of the dSphs used the same relation as used in this work). Another possibility is that the relation between core and soliton size is not as straightforward as the one used in this analysis. These different relations can change the conclusions reached here. We should also bear in mind that a soliton core in recent FDM simulations is not static but keeps oscillating with amplitude as large as the order of core radius. (Veltmaat et al. 2018; Schive et al. 2020). This phenomenon is described theoretically in Li et al. (2021). This suggests that our analysis based on the simple steady-state modeling of FDM might not describe the FDM halo potential perfectly, which would alter the FDM mass constraints obtained in this work. Future simulations of the FDM model might help answer these questions. Most importantly, future simulations that include baryons and can test the effect of baryonic effects in the dSph halos would be important to understand this discrepancy between dSphs and other observations.

5. Conclusions

In this work, we scrutinized the FDM model through a dynamical analysis of 18 UFDs with the simulation-driven FDM halo density profile. In this work, we were able to put the strongest constraints to date on the FDM mass, with a preference for higher masses $m_\psi \gtrsim 10^{-21}$ eV, with the strongest one from Segue 1, $m_\psi = 1.1^{+8.3}_{-0.7} \times 10^{-19}$ (1σ) eV. This means that the core present in these UFDs is small and shows that for these galaxies, for which the kinematic data available cover a larger spatial extent than the obtained r_c, a density profile of a soliton core embedded in an NFW outer profile is needed. The our constraints are compatible with previous bounds from the literature, except classical dSphs (Fornax and Sculptor), a discrepancy already noted in the literature, which might come from baryonic feedback on the dark matter distribution in these luminous galaxies. As UFDs are hardly affected by baryonic effects, they are the ideal laboratory to test DM models. With the huge increase in the amount of high-quality spectroscopic and astrometric observations in the near future, it will be possible to use UFDs to improve on the constraints obtained here, showing the power of UFDs to help understand the nature of DM.

ORCID iDs

Kohei Hayashi ⬤ https://orcid.org/0000-0002-8758-8139
Elisa G. M. Ferreira ⬤ https://orcid.org/0000-0002-5032-8368
Hei Yin Jowett Chan ⬤ https://orcid.org/0000-0001-9053-6922

References

Armengaud, E., Palanque-Delabrouille, N., Yèche, C., Marsh, D. J., & Baur, J. 2017, MNRAS, 471, 4606
Baes, M., & Van Hese, E. 2007, A&A, 471, 419
Binney, J., & Tremaine, S. 2008, Galactic Dynamics (2nd ed.; Princeton, NJ: Princeton Univ. Press)
Burkert, A. 2020, ApJ, 904, 161
Calabrese, E., & Spergel, D. N. 2016, MNRAS, 460, 4397
Chen, S.-R., Schive, H.-Y., & Chiueh, T. 2017, MNRAS, 468, 1338
Davoudiasl, H., & Denton, P. B. 2019, PhRvL, 123, 021102
Drlica-Wagner, A., Bechtol, K., Rykoff, E. S., et al. 2015, ApJ, 813, 109
Ferreira, E. G. 2020, arXiv:2005.03254
Foreman-Mackey, D., Hogg, D. W., Lang, D., & Goodman, J. 2013, PASP, 125, 306
González-Morales, A. X., Marsh, D. J., Peñarrubia, J., & Ureña López, L. A. 2017, MNRAS, 472, 1346
Hayashi, K., Chiba, M., & Ishiyama, T. 2020, ApJ, 904, 45
Hayashi, K., & Obata, I. 2020, MNRAS, 491, 615
Hlozek, R., Grin, D., Marsh, D. J. E., & Ferreira, P. G. 2015, PhRvD, 91, 103512
Hlozek, R., Marsh, D. J. E., & Grin, D. 2018, MNRAS, 476, 3063
Hu, W., Barkana, R., & Gruzinov, A. 2000, PhRvL, 85, 1158
Hui, L. 2021, arXiv:2101.11735
Hui, L., Ostriker, J. P., Tremaine, S., & Witten, E. 2017, PhRvD, 95, 043541
Iršič, V., Viel, M., Haehnelt, M. G., Bolton, J. S., & Becker, G. D. 2017, PhRvL, 119, 031302
Jenkins, S., Li, T. S., Pace, A. B., et al. 2020, arXiv:2101.00013

Kirby, E. N., Boylan-Kolchin, M., Cohen, J. G., et al. 2013, ApJ, 770, 16
Kirby, E. N., Cohen, J. G., Simon, J. D., et al. 2017, ApJ, 838, 83
Kirby, E. N., Simon, J. D., & Cohen, J. G. 2015, ApJ, 810, 56
Lazar, A., Bullock, J. S., Boylan-Kolchin, M., et al. 2020, MNRAS, 497, 2393
Li, X., Hui, L., & Yavetz, T. D. 2021, PhRvD, 103, 023508
Marsh, D. J., & Niemeyer, J. C. 2019, PhRvL, 123, 051103
Marsh, D. J. E., & Pop, A.-R. 2015, MNRAS, 451, 2479
Mina, M., Mota, D. F., & Winther, H. A. 2020, arXiv:2007.04119
Mocz, P., Lancaster, L., Fialkov, A., Becerra, F., & Chavanis, P.-H. 2018, PhRvD, 97, 083519
Mocz, P., Vogelsberger, M., Robles, V. H., et al. 2017, MNRAS, 471, 4559
Moliné, A., Sánchez-Conde, M. A., Palomares-Ruiz, S., & Prada, F. 2017, MNRAS, 466, 4974
Muñoz, R. R., Patrick, C., Felioe, A. S., et al. 2018, ApJ, 860, 66
Nadler, E., Drlica-Wagner, A., Bechtol, K., et al. 2021, PhRvL, 126, 091101
Navarro, J. F., Frenk, C. S., & White, S. D. 1997, ApJ, 490, 493
Nori, M., Murgia, R., Iršič, V., Baldi, M., & Viel, M. 2019, MNRAS, 482, 3227
Plummer, H. C. 1911, MNRAS, 71, 460
Read, J., Walker, M., & Steger, P. 2019, MNRAS, 484, 1401
Rogers, K. K., & Peiris, H. V. 2021, PhRvL, 126, 071302
Safarzadeh, M., & Spergel, D. N. 2020, ApJ, 893, 21
Schive, H.-Y., Chiueh, T., & Broadhurst, T. 2014, NatPh, 10, 496
Schive, H.-Y., Chiueh, T., & Broadhurst, T. 2020, PhRvL, 124, 201301
Schutz, K. 2020, PhRvD, 101, 123026
Simon, J. D., & Geha, M. 2007, ApJ, 670, 313
Simon, J. D., Geha, M., Minor, Q. E., et al. 2011, ApJ, 733, 46
Simon, J., Drlica-Wagne, A., Li, T. S., et al. 2015, ApJ, 808, 95
Simon, J., Li, T. S., Drlica-Wagner, A., et al. 2017, ApJ, 838, 11
Simon, J., Li, T. S., Erkal, D., et al. 2020, ApJ, 892, 137
Stott, M. J., & Marsh, D. J. 2018, PhRvD, 98, 083006
Veltmaat, J., Niemeyer, J. C., & Schwabe, B. 2018, PhRvD, 98, 043509
Wheeler, C., Oñorbe, J., Bullock, J. S., et al. 2015, MNRAS, 453, 1305
Willman, B., Geha, M., Strader, J., et al. 2011, AJ, 142, 128
Zoutendijk, S. L., Brinchmann, J., Bouché, N. F., et al. 2021, arXiv:2101.00253